J Mater Sci (2011) 46:7098–7105
DOI 10.1007/s10853-011-5409-8

SIZE DEPENDENT EFFECTS

Nano-domain structure of $Li_4Mn_5O_{12}$ spinel

Sv. Ivanova · E. Zhecheva · D. Nihtianova · R. Stoyanova

Received: 20 December 2010 / Accepted: 17 February 2011 / Published online: 24 February 2011

Abstract XRD-pure $Li_4Mn_5O_{12}$ spinels are obtained below 600 °C from oxalate and acetate precursors. The morphology consists of nanometric particles (about 25 nm) with a narrow particle size distribution. HRTEM and electron paramagnetic resonance (EPR) spectroscopy of Mn^{4+} are employed for local structure analysis. The HRTEM images recorded on nano-domains in $Li_4Mn_5O_{12}$ reveal its complex structure. HRTEM shows one-dimensional structure images, which are compatible with the (111) plane of the cubic spinel structure and the (001) plane of monoclinic Li_2MnO_3. For $Li_4Mn_5O_{12}$ compositions annealed between 400 and 800 °C, EPR spectroscopy shows the appearance of two types of Mn^{4+} ions having different metal environments: (i) Mn^{4+} ions surrounded by Li^+ and Mn^{4+} and (ii) Mn^{4+} ions in Mn^{4+}-rich environment. The composition of the Li^+, Mn^{4+}-shell around Mn^{4+} mimics the local environment of Mn^{4+} in monoclinic Li_2MnO_3, while the Mn^{4+}-rich environment is related with that of the spinel phase. The structure of XRD-pure $Li_4Mn_5O_{12}$ comprises nano-domains with a Li_2MnO_3-like and a $Li_{4/3-x}Mn_{5/3+x}O_4$ composition rather than a single spinel phase with Li in tetrahedral and $Li_{1/3}Mn_{5/3}$ in octahedral spinel sites. The annealing of $Li_4Mn_5O_{12}$ at temperature higher than 600 °C leads to its decomposition into monoclinic Li_2MnO_3 and spinel $Li_{4/3-x}Mn_{5/3+x}O_4$.

Sv. Ivanova · E. Zhecheva (✉) · D. Nihtianova · R. Stoyanova
Institute of General and Inorganic Chemistry, Bulgarian
Academy of Sciences, 1113 Sofia, Bulgaria
e-mail: zhecheva@svr.igic.bas.bg

D. Nihtianova
Institute of Mineralogy and Crystallography, Bulgarian
Academy of Sciences, Acad. G. Bonchev Str. bl. 107,
1113 Sofia, Bulgaria

Introduction

Lithium manganese oxides with spinel and layered structure are one of the most intensively studied during the last 15 years electrode materials for lithium–ion batteries [1, 2]. Layered manganese oxides display higher lithium mobility, while spinel manganese oxides are structurally more stable at a lower lithium content [3–5]. The possible intergrowth between the layered and spinel structures opens a new direction in the design of electrode materials. Recently, Thackeray et al. [3] have reported that monoclinic Li_2MnO_3 can be structurally integrated into $Li_{4/3}Mn_{5/3}O_4$ spinel forming $Li_2MnO_3\cdot(1-x)Li_{4/3}Mn_{5/3}O_4$ composites, which have a better electrochemical performance as compared to the single spinel manganese phase [3]. The structural integration takes place at an atomic level due to the structural similarity of the oxygen sub-lattices. The $Li_{4/3}Mn_{5/3}O_4$ composition (or $Li_4Mn_5O_{12}$) is described as a single phase with a cubic spinel structure, in which the lithium ions occupy the tetrahedral *8a* and part of the octahedral *16d* spinel sites, while the manganese ions reside in the octahedral *16d* sites (space group *Fd3m*). In the spinel notation, the structural formula of $Li_4Mn_5O_{12}$ is denoted by $Li[Li_{1/3}Mn_{5/3}]O_4$. The crystal structure of Li_2MnO_3 ($C2/m$ space group) consists of alternating (Li_2) and ($LiMn_2$) layers in which the MO_6 octahedra share common edges [6–8]. The structural formula of Li_2MnO_3 can be described as $Li[Li_{1/3}Mn_{2/3}]O_2$. In the monoclinic $Li[Li_{1/3}Mn_{2/3}]O_2$ phase the lithium and the manganese ions are ordered inside the layers, while they are randomly distributed in the *16d* sites of the $Li_{4/3}Mn_{5/3}O_4$ spinel.

The manganese ions in both monoclinic Li_2MnO_3 and spinel $Li_4Mn_5O_{12}$ phases adopt the oxidation state of 4+. Due to the structural instability of the Mn^{4+} ions, $Li_4Mn_5O_{12}$ is usually obtained at temperatures lower than

600 °C, since above 600 °C it decomposes into a lithium-poor spinel ($Li[Li_{1/3-x}Mn_{5/3+x}]O_4$ with $0 < x < 1/3$) and Li_2MnO_3 [9–14]. The low-temperature synthesis methods including solution-based and solid state reactions lead usually to the formation of nano-sized $Li_4Mn_5O_{12}$ spinels [12–14]. It is worth to mention that phase-pure stoichiometric (in respect of the Li-to-Mn ratio) $Li_4Mn_5O_{12}$ is still not prepared [15]. The structure of Li_2MnO_3 is also sensitive towards the synthesis temperature [8, 16, 17]. Li_2MnO_3 with a lower degree of defects is obtained at 900 °C, while at lower temperatures a disordering of the stacking of $Li_{1/3}Mn_{2/3}$ layers along the monoclinic direction becomes more significant [16, 17].

Taking into account the structural resemblance between the spinel and the Li_2MnO_3 structure as well as the low preparation temperature of the $Li_4Mn_5O_{12}$ composition, a detailed knowledge on the local structure of Mn^{4+} ions is required which is of importance for the electrochemical properties on this oxide [5, 18]. EPR spectroscopy is well suited for studying the local structure of transition metal ions in layered and spinel phases [19–29]. From an EPR point of view, the local structure comprises mainly the first coordination metal sphere [19]. Whereas the EPR signal for Li_2MnO_3 corresponds to exchange coupled Mn^{4+} ions, the collective Mn^{4+} and Mn^{3+} system contributes to the EPR response of $Li_{1+x}Mn_{2-x}O_4$ spinels with $0 \leq x \leq 0.1$. As a result, the EPR line width increases from 21 to 220 mT for Li_2MnO_3 and $Li_{1+x}Mn_{2-x}O_4$, respectively [26, 27]. In the case of $Li_4Mn_5O_{12}$, analysis of the EPR line width in terms of magnetic dipole–dipole and exchange interactions reveals the appearance of two kinds of Mn^{4+} in octahedral spinel sites: one of them has as first neighbours five paramagnetic Mn^{4+} and one diamagnetic Li^+, whereas the second type of Mn^{4+} is in a Li-rich surrounding [26].

The aim of this contribution is to study by EPR the local structure of Mn^{4+} in nano-sized $Li_4Mn_5O_{12}$ as a function of the annealing temperature. For the synthesis of lithium-manganese oxides, we have adopted two methods: the oxalate and the acetate precursor methods. The oxalate precursor method has been shown to be suitable for the preparation of nano-sized lithium manganese spinels [30–32]. The acetate precursor method is based on the freeze-drying process, which enables the preparation of homogeneous and well-crystallized lithium transition metal oxides [23, 33]. Powder XRD, SEM, and TEM analysis are employed for structural and morphological characterization of the spinel compositions. The information on the local structure of Mn^{4+} is extracted by comparative analysis of the EPR line width with that of the monoclinic Li_2MnO_3 which were used as EPR standards.

Experimental

The oxalate precursors were synthesized by a room temperature solid state reaction based on the procedure used by Ye et al. [30]. According to this method, lithium hydroxide and oxalic acid were mixed in a molar ratio of 1:1 and then ground in agate mortar until the mixture became sticky, then solid manganese acetate was added. Heating up to 400 °C removed the adsorbed water and acetic acid, followed by thermal decomposition of the precursor. The decomposition products were annealed in the temperature range of 400–800 °C for 10 h.

The acetate precursor method consists in freeze-drying of aqueous solutions of lithium and manganese acetates, followed by thermal decomposition at 400 °C in air. The concentration of the solution was 0.5 M with respect to the metal content. The solution was cooled down to room temperature, then frozen instantly with liquid nitrogen and dried in vacuum (20–30 mbars) at −20 °C with an Alpha-Crist Freeze-Dryer. The freeze-dried product was decomposed at 400 °C, followed by annealing in the temperature range of 400–800 °C for 10 h.

The lithium content of the samples was determined by atomic absorption analysis. The total amount of manganese was determined complexometrically and by atomic absorption analysis. The mean oxidation state of manganese in the oxide samples was determined by permanganometric titration.

The X-ray structural analysis was made by Bruker Advance D8 powder diffractometer with Cu K_α radiation. The scan range was $15 \leq 2\theta \leq 120$ with a step increment of 0.02°. A Fullprof computer software was used for the calculations [34]. The diffractometer zero point, the Lorentzian/Gaussian fraction of the pseudo-Voigt peak function, scale factor, the unit cell parameters, the oxygen parameter, the thermal factor for the spinel atomic positions, the line half-width parameters and the preferred orientation were determined. The Li and Mn amount in the *16d* position was refined taking into account that the total occupancy is equal to 1.

The EPR spectra were recorded as the first derivative of the absorption signal of an ERS-220/Q spectrometer within the temperature range of 90–400 K. The g factors were determined with respect to a Mn^{2+}/ZnS standard. The signal intensity was established by double integration of the experimental EPR spectrum.

The TEM investigations were performed on a TEM JEOL 2100 instrument at accelerating voltage of 200 kV. The specimens were prepared by grinding and dispersing them in ethanol by ultrasonic treatment for 6 min. The suspensions were dripped on standard holey carbon/Cu grids. The measurements of lattice-fringe spacing recorded in HRTEM micrographs were made using digital image analysis of reciprocal space parameters [34]. The analysis was carried out by the Digital Micrograph software.

Results and discussion

Structural and morphological analysis of $Li_4Mn_5O_{12}$

Figure 1 shows the XRD patterns of $Li_4Mn_5O_{12}$ after heat treatment between 400 and 800 °C. At 400 °C, a single spinel phase is formed. The oxidation state of Mn ions is slightly lower than 4 (Table 1). The XRD pattern is satisfactory fitted by the Rietveld analysis on the basis of the model of the spinel structure including Li in both tetrahedral *8a* and octahedral *16d* sites and Mn in *16d p*ositions only (Fig. 1, Table 1). This is the structural model that is used for the interpretation of the spinel structure of $Li_4Mn_5O_{12}$ [9, 10]. The refined amount of Li in *16d* is slightly lower than 1/3 (Table 1), thus confirming the formation of pure spinel phase $Li_4Mn_5O_{12}$. The structural formulae correspond to $[Li]_{8a}[Li_{0.264}Mn_{1.736}]_{16d}[O_4]_{32e}$, $[Li]_{8a}[Li_{0.260}Mn_{1.740}]_{16d}[O_4]_{32e}$ and $[Li]_{8a}[Li_{0.252}Mn_{1.748}]_{16d}[O_4]_{32e}$ for samples annealed at 400, 600 and 800 °C, respectively.

The spinel phase is preserved after further heating up to 600 °C (Fig. 1). In this temperature range, the unit cell parameter displays a tendency to increase (Fig. 2). Above 600 °C, additional reflections due to impurity Li_2MnO_3 phase become visible in the XRD patterns of $Li_4Mn_5O_{12}$ (Fig. 1). This is concomitant with a strong increase in the unit cell parameter of $Li_4Mn_5O_{12}$ (Fig. 2). The same tendency in the temperature induced changes of the unit cell parameter has been established for $Li_4Mn_5O_{12}$ and has been explained with the structural instability of the Mn^{4+} ions at higher temperatures [10]. The reduction of Mn^{4+} to Mn^{3+} ions causes an extraction of Li from the *16d* spinel sites together with the release of Li_2MnO_3 [10].

To understand whether $Li_4Mn_5O_{12}$ is a single phase or a composite, SEM and TEM analysis are undertaken. At 400 °C, dense aggregates are formed (Fig. 3). Inside the aggregates, well-crystallized thin hexagonal particles become visible (Fig. 4). The polycrystalline electron diffraction reveals the formation of spinel phase with lattice parameter close to that determined by XRD: 8.149 versus 8.1548 Å. The particle dimensions fall into the nanometric scale and display a close size distribution: more then 70% of the particles are between 15 and 30 nm (Fig. 4). The crystallite size estimated from the broadening of the (111) peak is around 28 nm. The close values of the particle dimensions and the XRD crystallite sizes confirm the formation at 400 °C of nano-sized well-crystallized $Li_4Mn_5O_{12}$.

The HRTEM images of $Li_4Mn_5O_{12}$ are shown in Fig. 5. The lattice-fringes images recorded on nano-domains in $Li_4Mn_5O_{12}$ reveal its complex structure. The two-dimensional HRTEM image corresponding to the (111) spinel plane is well resolved. The one-dimensional HRTEM images consist of lattice fringes corresponding to a *d*-value of about 4.7 Å. This value is equivalent to the interplanar spacing of the (111) plane in the cubic spinel structure (4.71 Å). However, the *d*-value of the (001) plane of monoclinic Li_2MnO_3 is also similar (4.74 Å). This means that the presence of nano-domains of monoclinic Li_2MnO_3 cannot be excluded. Therefore, from HRTEM images we

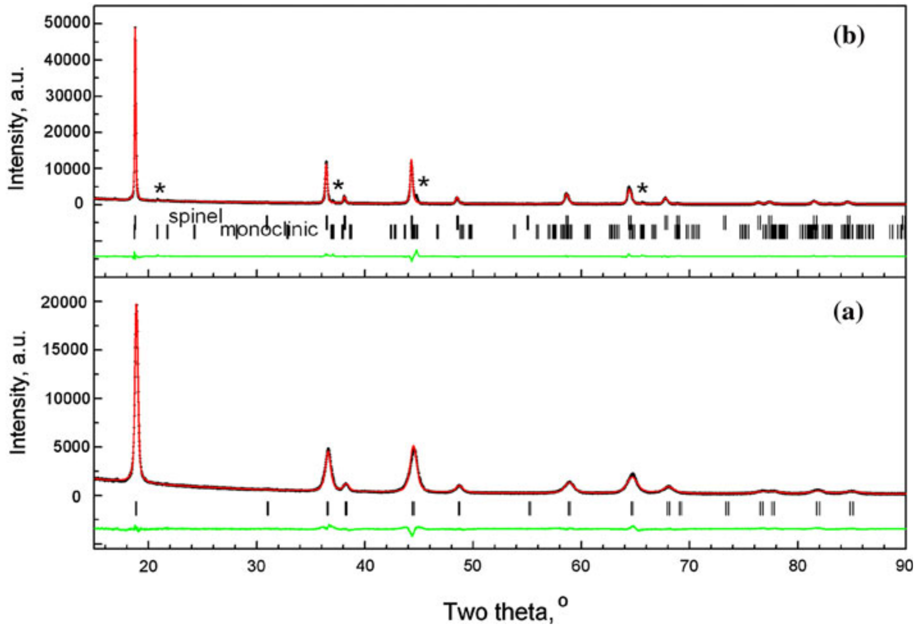

Fig. 1 XRD patterns of $Li_4Mn_5O_{12}$ annealed at 400 (**a**) and 800 °C (**b**). The *asterisk* denotes the most intensive diffraction peaks due to monoclinic Li_2MnO_3 phase. Bragg reflections for spinel oxides and monoclinic Li_2MnO_3 are indicated

Table 1 Oxidation state of manganese ions (OS) and structural parameters of $Li_4Mn_5O_{12}$ annealed at 400, 600 and 800 °C (T_{ann})

T_{ann} (°C)	OS (±0.03)	a (Å) (±0.0003)	z, oxygen parameter	Li in [*16d*]	B_{8a}, Å^2	B_{16d}, Å^2	B_{32e}, Å^2	R_B	R_f	Fraction (%)
400	3.98	8.1548	0.2628 (2)	0.132 (4)	0.65	0.54	0.92	3.54	2.64	–
600	3.99	8.1643	0.2629 (1)	0.130 (4)	0.65	0.47	1.37	3.15	1.94	–
800	3.92	8.1771	0.2632 (2)	0.126 (4)	0.59	0.50	1.26	3.48	2.62	2.08 (1)

The fraction of Li_2MnO_3 is also included

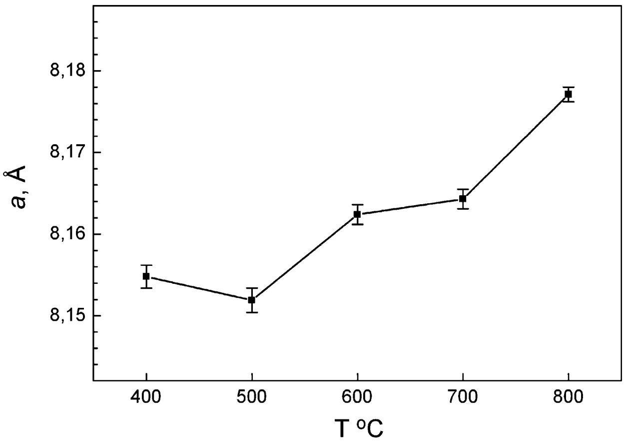

Fig. 2 Unit cell parameter versus the annealing temperature of annealing

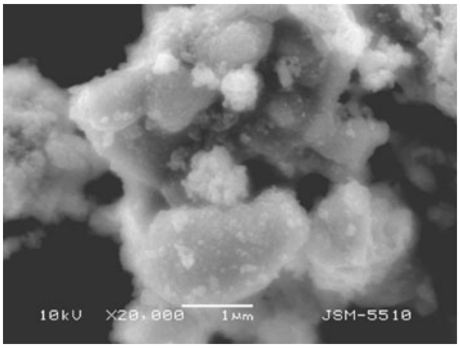

Fig. 3 SEM images of $Li_4Mn_5O_{12}$ annealed at 400 °C

cannot unambiguously conclude if $Li_4Mn_5O_{12}$ is a single spinel phase or presents nano-domains with a Li_2MnO_3-like and a $Li_{4/3-x}Mn_{5/3+x}O_4$ spinel composition forming a composite structure. Similar HRTEM images were observed by Thackeray et al. on lithium–manganese oxide electrodes with the composition $0.7Li_2MnO_3{\cdot}3Li_4Mn_5O_{12}$ and they have regarded the sample as a composite product containing nano-domains of structurally integrated layered and spinel phases [3]. In addition, some nano-domain regions in the HRTEM image in Fig. 5 show that the (111) plane is warped like to 'artificial' moiré fringes [35]. By increasing the annealing temperature, particle growth takes place, as a result of which hexagonal particles with dimensions between 150 and 350 nm are formed (Fig. 6). Selected area electron diffraction (SAED) reveals the presence of a spinel phase at 800 °C (Fig. 7).

EPR spectroscopy of $Li_4Mn_5O_{12}$

EPR of Mn^{4+} is used as an experimental tool for monitoring the local structure of Mn^{4+} in $Li_4Mn_5O_{12}$ compositions annealed between 400 and 800 °C (Fig. 8). The EPR spectra of all samples consist of two overlapping Lorentzian lines having different g-values and line widths. The broad signal with a g-factor of 2.02 dominates the EPR profiles of the spinels obtained at 400 °C, while the narrow signal with a g-factor of 1.99 is well resolved in the spectrum of $Li_4Mn_5O_{12}$ obtained at 800 °C. Between 400 and 800 °C, there is a progressive change in the intensity ratios of the two signals. In the temperature range of

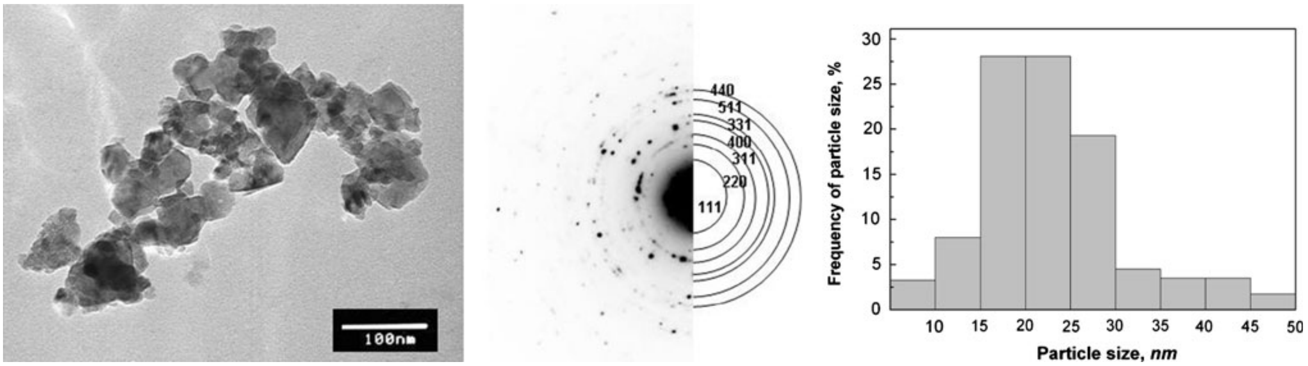

Fig. 4 Bright field micrograph of $Li_4Mn_5O_{12}$ obtained at 400 °C and polycrystalline electron diffraction corresponding to the spinel phase ($a = 8.149$ Å)

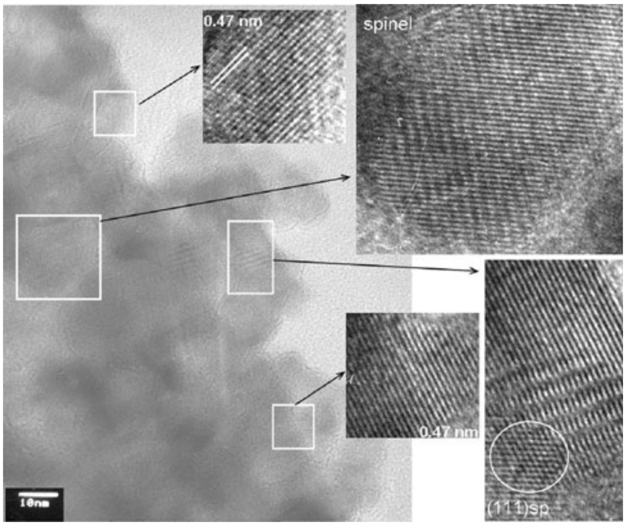

Fig. 5 HRTEM images of $Li_4Mn_5O_{12}$ obtained at 400 °C. The *insets* are Fourier filtered HRTEM images

100–410 K, the *g*-factor of the narrow signal remains constant, while the *g*-factor of the broad signal tends to increase on cooling: from 2.024(3) to 2.032(3) when going from 413 to 103 K. Figure 9 compares the temperature dependence of the EPR line widths of the narrow and the broad signals. Both signals are characterized with line widths that depend on the recording temperature in a different way: the line width of the narrow signal increases with decreasing of the recording temperature, while the line width of the broad signal decreases (Fig. 9). Furthermore, the values of the line widths are sensitive towards the annealing temperature of the oxides. The line width of the narrow signal (Signal 1) decreases with increasing the annealing temperature, at difference with the line width of the broad signal (Signal 2) which increases (Fig. 10).

The same two EPR signals have already been detected in $Li_4Mn_5O_{12}$ obtained by solid state reaction at 400 °C [26]. These signals have been attributed to Mn^{4+} ions,

Fig. 6 Bright field micrograph of $Li_4Mn_5O_{12}$ obtained at 800 °C

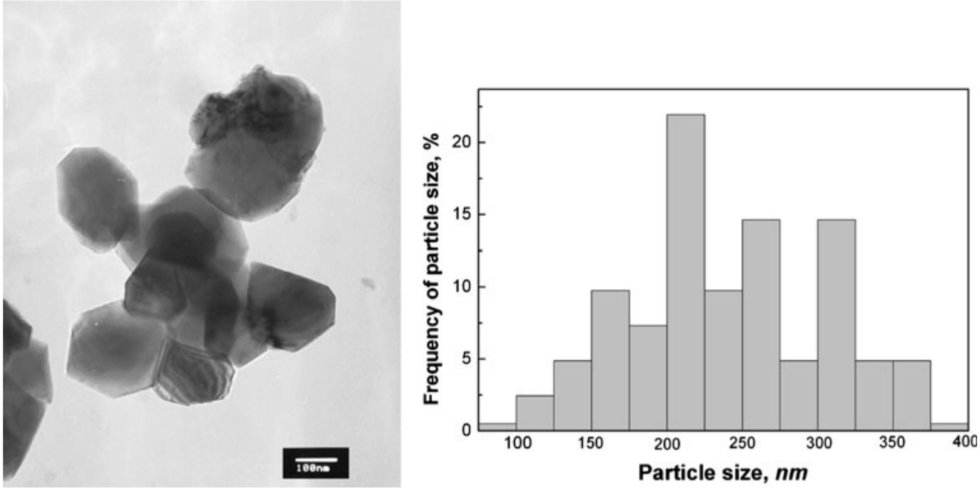

Fig. 7 Bright field micrograph of $Li_4Mn_5O_{12}$ obtained at 800 °C. Selected area electron diffraction (SAED) of the particle along [110] orientation in the spinel structure

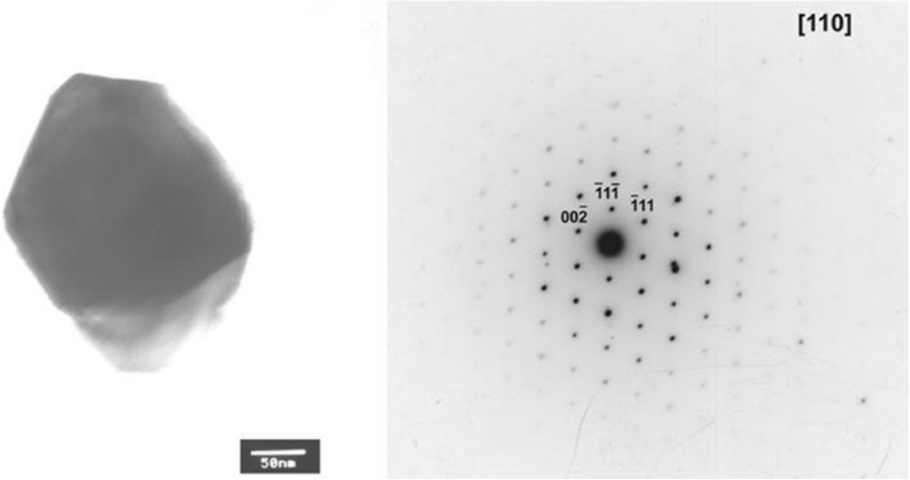

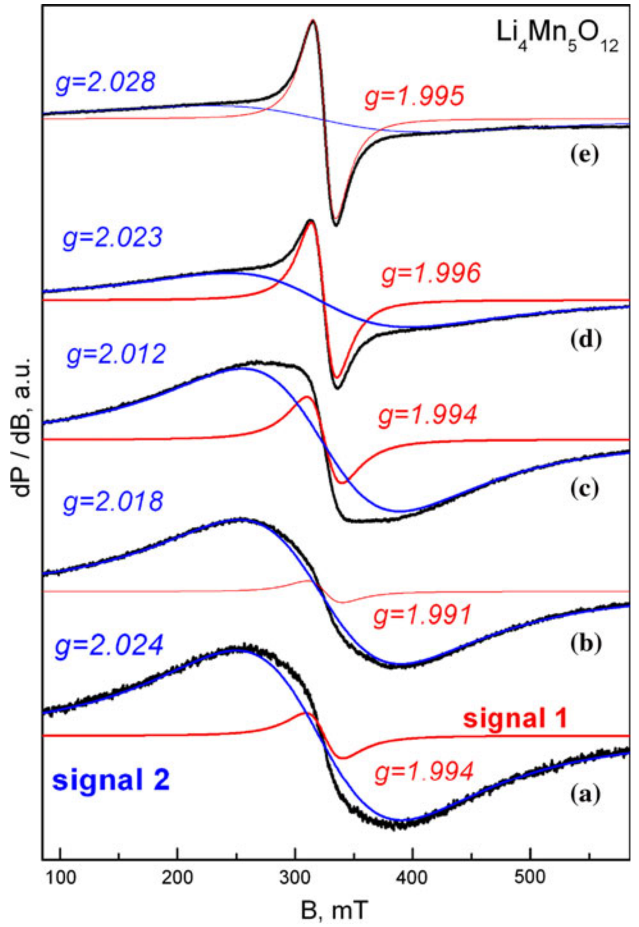

Fig. 8 EPR spectra at 413 K of $Li_4Mn_5O_{12}$ annealed at 400, 500, 600, 700 and 800 °C. The experimental EPR spectrum (*thick/black lines*) is deconvoluted into two signals having the Lorentzian line shapes (*thin/red lines*, signal 1 and *thin/blue lines*, signal 2) (Color figure online)

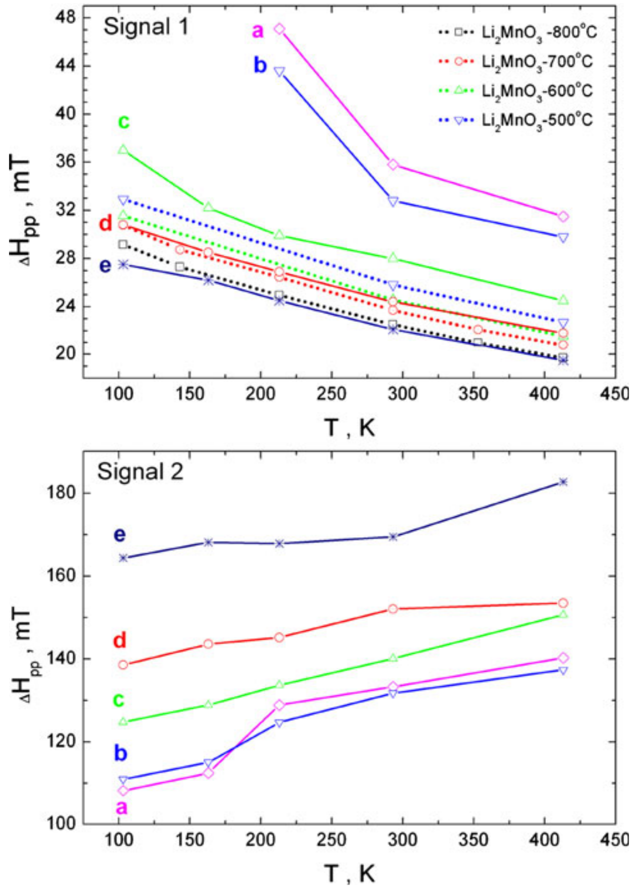

Fig. 9 Temperature evolution of the EPR line width of narrow and broad signals (signals 1 and 2) of $Li_4Mn_5O_{12}$ annealed at 400, 500, 600, 700 and 800 °C. For the sake of comparison, the temperature evolution of the EPR line width of Li_2MnO_3 annealed at 500, 600, 700 and 800 °C is also shown

which can be differentiated on the basis of their metal environment: the narrow signal comes from Mn^{4+} ions located in a mixed Li^+/Mn^{4+} environment, while the broad signal is due to Mn^{4+} ions in a Mn^{4+}-rich environment [26]. The new finding is the dependence of the EPR line widths on the annealing temperature (Fig. 10). This means that the composition of the coordination sphere of Mn^{4+} ions in $Li_4Mn_5O_{12}$ is changed during the annealing.

To understand the local structure of Mn^{4+} ions in $Li_4Mn_5O_{12}$, the EPR spectrum of Li_2MnO_3 is also taken into account. As was recently demonstrated [26, 36], the EPR spectrum of Li_2MnO_3 displays only one narrow Lorentzian line with *g*-factor of 1.99. This signal is due to Mn^{4+} ions located in the environment of paramagnetic Mn^{4+} and diamagnetic Li^+ ions. In the $(Li_{1/3}Mn_{2/3})$ layers, the manganese ions are coupled by antiferromagnetic interactions (via oxygen), as a result of which the signal is broadened on cooling. This is what we observe for Li_2MnO_3 annealed between 500 and 800 °C (Fig. 9). As in the case of $Li_4Mn_5O_{12}$, the EPR line width of Mn^{4+} depends on the annealing temperature (Fig. 10): the line width decreases with increasing the annealing temperature. The observed changes in the line width can be related with the defect structure of Li_2MnO_3. Recently, it has been shown that the higher annealing temperature favours the formation of Li_2MnO_3 with a lower degree of disordering of the $Li_{1/3}Mn_{2/3}$ layers along the *c* monoclinic direction [26, 36]. Therefore, one can suggest that the more Li_2MnO_3 is defective, the more broadened is the EPR signal.

Comparison of the EPR spectra of Li_2MnO_3 and $Li_4Mn_5O_{12}$ confirms once again that the narrow signal originates from Mn^{4+} ions having Mn^{4+} and Li^+ ions as neighbours. It is noticeable that for spinels annealed between 400 and 600 °C the line width of the narrow signal is higher in comparison with that of the signal of Mn^{4+} in Li_2MnO_3 (Fig. 10). This means that the Mn^{4+} ions are surrounded by Li^+ and Mn^{4+} ions in a ratio that mimics the composition of the local environment for Mn^{4+} in Li_2MnO_3. When the spinels are annealed at a temperature

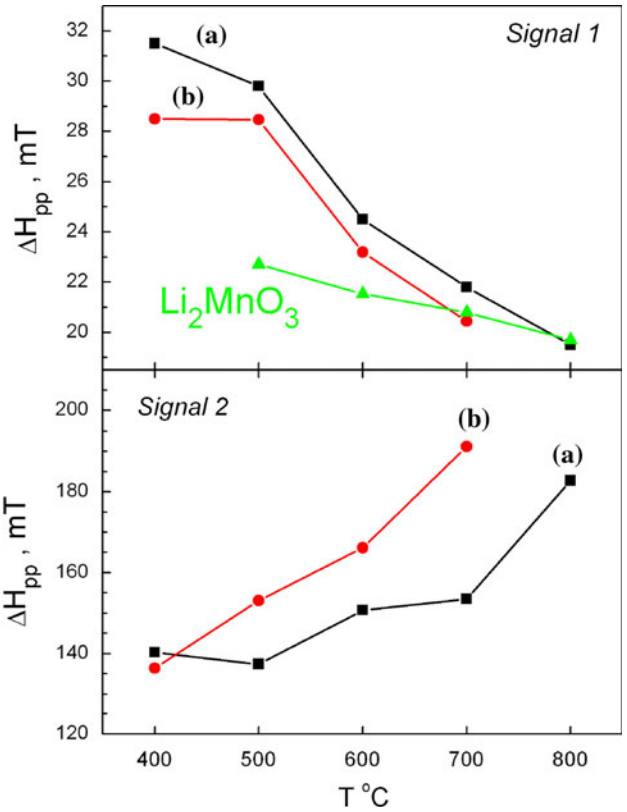

Fig. 10 EPR line width of narrow and broad signals (signals 1 and 2) of $Li_4Mn_5O_{12}$ obtained by oxalate (**a**) and acetate (**b**) precursor methods as a function of the annealing temperature. For the sake of comparison, the EPR line width of Li_2MnO_3 is also given

higher than 600 °C, the narrow signal of $Li_4Mn_5O_{12}$ and the signal of Mn^{4+} in Li_2MnO_3 display one and same line width (Fig. 10). This indicates that the composition of the local environment for Mn^{4+} ions in both $Li_4Mn_5O_{12}$ and Li_2MnO_3 oxides is identical. This can be explained in terms of the release of a separate phase Li_2MnO_3 when the spinels are annealed above 600 °C. For the same samples, a monoclinic Li_2MnO_3 phase is also detected by XRD (Fig. 1).

The second signal undergoes a significant broadening when the spinels are annealed at higher temperatures. This reveals compositional changes in the coordination sphere of the Mn^{4+} ions in the Mn^{4+}-rich environment. By increasing the annealing temperature, it appears that more and more Mn^{4+} ions are including into the coordination sphere of Mn^{4+} ions leading to the increase in the EPR line width (Fig. 10). In addition, the oxidation state of manganese ions for all $Li_4Mn_5O_{12}$ samples is slightly lower than 4 (Table 1). This means that a possible contribution of non-identical Mn^{3+} ions into the EPR line width of the broader signal due to Mn^{4+} ions cannot be rejected. For lithium manganese spinels, it has been shown that the density of the identical and the non-identical paramagnetic ions leads to an increase of the EPR line width in the case when antiferro- or ferromagnetic interactions are dominant [20]. On the contrary, when the strengths of antiferro- and ferromagnetic interactions are close, the EPR line width becomes broader and appears insensitive to the density of the paramagnetic species [20]. Based on magnetic susceptibility measurements, it has been shown that superexchange ferromagnetic interactions dominate for spinels where the Mn–Mn distance is higher than 2.86 [37], while an antiferromagnetic character is reported for spinels with a Mn–Mn distance lower than 2.85 Å [37, 38]. For $Li_4Mn_5O_{12}$ compositions, the distance between the manganese ions varies between 2.88 and 2.89 Å ($a\sqrt{2}/4$, Table 1), which is near to the crossover between the ferromagnetic and antiferromagnetic transition. This makes difficulties to quantify the effect of Mn^{4+} and Mn^{3+} on the EPR line width of the Mn^{4+} ions in $Li_4Mn_5O_{12}$. However, the significant difference in the line widths of the two EPR signals of $Li_4Mn_5O_{12}$ (more than five times, Fig. 10) indicate clearly that the Mn^{4+} ions are in different metal environments.

Therefore, one can conclude that below 600 °C the structure of $Li_4Mn_5O_{12}$, being a XRD-pure phase, consists of nano-domains with a Li_2MnO_3-like and $Li_{4/3-x}Mn_{5/3+x}O_4$ composition. Above 600 °C, this complex domain structure is decomposed with the release of a separate distinct Li_2MnO_3 phase. The appearance of an impurity Li_2MnO_3 phase has also been detected by muon-spin rotation/relaxation measurement [15]. To rationalize whether the nano-domain structure of $Li_4Mn_5O_{12}$ is dependent on the synthesis method, Fig. 10 compares the EPR line widths of the two signals of $Li_4Mn_5O_{12}$ obtained by the oxalate and acetate precursor methods. While the EPR line widths of the two samples are different, the dependence of the EPR line width on the annealing temperature remains the same. This reveals that the nano-domain structure of $Li_4Mn_5O_{12}$ is sensitive towards the history of the method of synthesis including the type of precursor used and the annealing temperature.

Conclusions

XRD-pure $Li_4Mn_5O_{12}$ spinel is prepared below 600 °C by the oxalate and acetate precursor methods. At 400 °C, the oxalate precursor method yields a $Li_4Mn_5O_{12}$ spinel with particle dimensions varying between 15 and 30 nm. HRTEM and EPR spectroscopy reveal that the structure of the nano-sized $Li_4Mn_5O_{12}$ spinel consists of nano-domains with a Li_2MnO_3-like and $Li_{4/3-x}Mn_{5/3+x}O_4$ compositions rather than a single spinel phase with Li in tetrahedral sites and $Li_{1/3}Mn_{5/3}$ in octahedral sites. The annealing of $Li_4Mn_5O_{12}$ at temperature higher than 600 °C leads to its decomposition into monoclinic Li_2MnO_3 and spinel $Li_{4/3-x}Mn_{5/3+x}O_4$. These results demonstrate the ability of the EPR spectroscopy to monitor the nano-domain structure of $Li_4Mn_5O_{12}$ as a function of annealing temperature and the type of the precursor used.

Acknowledgements Authors are grateful to the financial support from the National Science Fund of Bulgaria (Ch1701/2007). Partial financial support by the National Centre for New Materials UNION (Contract No DCVP-02/2/2009) is also acknowledged.

References

1. Whittingham MS (2004) Chem Rev 104:4271
2. Ellis BL, Lee KT, Nazar LF (2010) Chem Mater 22:691
3. Johnson CS, Li N, Vaughey JT, Hackney SA, Thackeray MM (2005) Electrochem Comm 7:528
4. Thackeray MM, Johnson CS, Vaughey JT, Li N, Hackney SA (2005) J Mater Chem 15:2257
5. Cabana J, Johnson CS, Yang XQ, Chung KY, Yoon WS, Kang SH, Thackeray MM, Grey CP (2010) J Mater Res 25:1601
6. Strobel P, Lambert-Anderson B (1988) J Solid State Chem 75:90
7. Riou A, Lecerf A, Gerault Y, Cudennec Y (1992) Mater Res Bull 27:269
8. Lei CH, Wen JG, Sardela M, Bareño J, Petrov I, Kang S-H, Abraham DP (2009) J Mater Sci 44:5579. doi:10.1007/s10853-009-3784-1
9. Thackeray MM, De Kock A, David WIF (1993) Mater Res Bull 28:1041
10. Takada T, Hayakawa H, Akiba E (1995) J Solid State Chem 115:420
11. Zhang Y, Wang H, Wang B, Yan H, Ahnyiaz A, Yoshimura M (2002) Mater Res Bull 37:1411
12. Tian Y, Chen D, Jiao X, Duan Y (2007) Chem Commun 2072
13. Zhao Y, Xu X, Lai Q, Hao Y, Wang L, Lin Z (2010) J Solid State Electrochem 14:1509
14. Jiang YP, Xie J, Cao GS, Zhao XB (2010) Electrochim Acta 56:412
15. Mukai K, Sugiyama J, Ikedo Y, Nozaki H, Kamazawa K, Andreica D, Amato A, Manson M, Brewer JH, Ansaldo EJ, Chow KH (2010) J Phys Chem C 114:11320
16. Boulineau A, Croguennec L, Delmas C, Weill F (2009) Chem Mater 21:4216
17. Boulineau A, Croguennec L, Delmas C, Weill F (2010) Solid State Ion 180:1652
18. Zhecheva E, Stoyanova R, Alcántara R, Lavela P, Tirado JL (2002) Pure Appl Chem 74:1885
19. Stoyanova R, Zhecheva E, Alcántara R, Lavela P, Tirado JL (1997) Solid State Commun 102:457
20. Zhecheva E, Stoyanova R (2005) Solid State Commun 135:405
21. Capsoni D, Bini M, Chiodelli G, Massarotti V, Mozatti MC, Comin A (2001) Phys Chem Chem Phys 3:2162
22. Capsoni D, Bini M, Chiodelli G, Massarotti V, Mozatti MC, Azzoni C (2003) Solid State Commun 125:179
23. Zhecheva E, Gorova M, Stoyanova R (1999) J Mater Chem 9:1559
24. Stoyanova R, Zhecheva E, Gorova M (2000) J Mater Chem 10:1377
25. Zhecheva E, Stoyanova R, Gorova M, Lavela P, Tirado JL (2001) Solid State Ion 140:19
26. Stoyanova R, Gorova M, Zhecheva E (2000) J Phys Chem Solids 61:615
27. Stoyanova R, Gorova M, Zhecheva E (2000) J Phys Chem Solids 61:609
28. Stoyanova R, Zhecheva E, Vassilev S (2006) J Solid State Chem 179:378
29. Stoyanova R, Zhecheva E, Alcántara R, Tirado JL (2006) J Mater Chem 16:359
30. Ye XR, Jia DZ, Yu JQ, Xin XQ, Xue Z (1999) Adv Mater 11:941
31. Huang Y, Li J, Jia D (2005) J Colloid Interface Sci 286:263
32. Tang X-C, Jiang C-K, Pan C-Y, Huang B-Y, He Y-H (2006) J Solid State Chem 179:1100
33. Alcántara R, Lavela P, Tirado JL, Stoyanova R, Kuzmanova E, Zhecheva E (1997) Chem Mater 9:2145
34. Rodríguez-Carvajal J (1990) In: Satellite meeting on powder diffraction of the XV congress of the IUCr, p 127
35. Williams DB, Carter CB (1996) Transmission electron microscopy, a textbook for materials science, basics I, diffraction II, imaging III. Plenum Press, New York, London
36. Massarotti V, Capsoni D, Bini M, Azzoni CB (1997) J Solid State Chem 128:80
37. Branford W, Green MA, Neumann DA (2002) Chem Mater 14:1649
38. Greedan JE, Raju NP, Wills AS, Morin C, Shaw SM, Reimers JN (1998) Chem Mater 10:3058